Seo et al. *NPG Asia Materials* (2020) 12:7
https://doi.org/10.1038/s41427-019-0186-y

NPG Asia Materials

ARTICLE Open Access

Artificially engineered nanostrain in $FeSe_xTe_{1-x}$ superconductor thin films for supercurrent enhancement

Sehun Seo[1], Heesung Noh[1], Ning Li[2], Jianyi Jiang[3], Chiara Tarantini[3], Ruochen Shi[2], Soon-Gil Jung[4], Myeong Jun Oh[5], Mengchao Liu[2], Jongmin Lee[1], Genda Gu[6], Youn Jung Jo[5], Tuson Park[4], Eric E. Hellstrom[3], Peng Gao[2] and Sanghan Lee[1]

Abstract

Although nanoscale deformation, such as nanostrain in iron-chalcogenide ($FeSe_xTe_{1-x}$, FST) thin films, has attracted attention owing to its enhancement of general superconducting properties, including critical current density (J_c) and critical transition temperature, the development of this technique has proven to be an extremely challenging and complex process thus far. Herein, we successfully fabricated an epitaxial FST thin film with uniformly distributed nanostrain by injection of a trace amount of CeO_2 inside an FST matrix using sequential pulsed laser deposition. By means of transmission electron microscopy and geometric phase analysis, we verified that the injection of a trace amount of CeO_2 forms nanoscale defects, with a nanostrained region of tensile strain ($\varepsilon_{zz} \cong 0.02$) along the *c*-axis of the FST matrix. This nanostrained FST thin film achieves a remarkable J_c of 3.5 MA/cm^2 under a self-field at 6 K and a highly enhanced J_c under the entire magnetic field with respect to those of a pristine FST thin film.

Introduction

Superconductors are essential materials for high magnetic field applications, such as those in nuclear fusion energy devices, magnetic resonance imaging, and superconducting magnetic energy storage systems. In recent years, iron-based superconductors (FeSCs) have attracted attention for use in high magnetic field applications because of their high upper-critical field (H_{c2}) and low magnetic anisotropy (γ)[1,2]. Moreover, FeSC epitaxial thin films have demonstrated enhanced overall superconducting properties compared with those of the corresponding bulk materials[3–9]. Among several FeSCs, iron chalcogenides ($FeSe_xTe_{1-x}$, FST), which are simple PbO-type chalcogenides with layered-like structures[10], are excellent candidates for use as practical superconducting materials for several reasons. First, the critical transition temperature (T_c) of FST abruptly increases due to an Se ratio that increases with the suppression of phase separation, which is generally observed in Se-rich FST bulk, when FST is fabricated as an epitaxial thin film[11,12]. In addition, an FeSe monolayer can achieve a T_c of 100 K, which is the maximum T_c for FeSCs[13]. Second, FST thin films exhibit promising critical current densities (J_c), greater than 1 MA/cm^2, under self-field regardless of the substrate, including coated conductor substrates[5,14]. This result indicates that these films can potentially be used as superconductor tape. However, J_c enhancement via an artificial pinning center is a critical requirement for use of FST in high magnetic field applications.

Several approaches have been used to improve the J_c of FST to date, such as the use of a buffer layer[14], oxygen annealing[15], and ion irradiation[16,17]. In particular, low-

Correspondence: Sanghan Lee (sanghan@gist.ac.kr)
[1]School of Materials Science and Engineering, Gwangju Institute of Science and Technology, Gwangju 61005, Republic of Korea
[2]Electron Microscopy Laboratory, and International Center for Quantum Materials, School of Physics, Peking University, 100871 Beijing, China
Full list of author information is available at the end of the article.
These authors contributed equally: Sehun Seo, Heesung Noh

energy proton irradiation (190 keV) is an effective method for this purpose because this method causes nanoscale cascade defects accompanied by nanostrain that simultaneously enhances both the T_c and J_c in an FST thin film[16]. However, proton irradiation is a complicated ex situ process that is not suitable for practical applications. Therefore, a straightforward in situ process for forming artificially controlled nanostrain is necessary to improve the J_c of FSTs.

Nanostrain has been generated via the introduction of various defect formations to date. For example, the insertion of a desired material with a slightly different lattice constant can induce strain through the formation of a secondary phase[18,19]; further, the doping of certain elements can generate lattice changes with nanoscale strain[20]. The formation of cascades[16] or point defects[21] by ion irradiation induces deformation of a lattice through nanoscale defects. In FST thin films, since large-scale and excessive numbers of defects can degrade the entire superconducting matrix[22] and FST has a short coherence length (~2 nm)[23], the formation of minimally sized defects is required for inducing nanostrain to prevent Cooper pair breaking while improving J_c.

Herein, we report that nanostrain was successfully formed in an epitaxial FST thin film through the formation of minimal nanoscale defects in an FST thin film using sequential pulsed laser deposition (S-PLD), which can artificially insert the desired material while fabricating an epitaxial thin film[4,24,25]. We injected precisely controlled trace amounts of CeO_2 to minimize the residual insertion of materials to form nanoscale defects. CeO_2 was used as an insertion material because CeO_2 exhibits not only good chemical stability but also an in-plane lattice constant compatible with that of FST[14,26–28], and hence, the degradation of superconductivity can be minimized rather than inserting other oxides, even if residual CeO_2 exists in FST. The crystallinity and structure of the CeO_2-injected FST (Ce-FST) were confirmed using X-ray diffraction (XRD) measurements. The nanostrain was analyzed using atomic-resolution scanning transmission electron microscopy (STEM) with geometric phase analysis (GPA). The nanostrained Ce-FST thin film exhibits a significantly enhanced J_c compared with that of a pristine FST (P-FST) thin film.

Materials and methods

Sample preparation

We fabricated both P-FST and Ce-FST thin films on a (001)-oriented CaF_2 substrate by PLD using a KrF (248 nm) excimer laser (Coherent, COMPEX PRO 205F) in a vacuum of 2×10^{-5} Pa at 400 °C. We used an $FeSe_{0.45}Te_{0.55}$ target made by an induction melting method. The FST thin films were grown using a laser energy density of 3 J/cm^2, a pulse repetition rate of 3 Hz, and a target-to-substrate distance of 4 cm.

The method for fabricating the Ce-FST thin films is as follows. We first deposited a 20-nm (445 laser pulses) FST layer on the CaF_2 substrate. Then, CeO_2 was deposited on the FST layer.

These processes were repeated four times in total, and finally, an FST layer was deposited on the top surface. The total thickness of all the FST thin films was 100 nm (2225 laser pulses).

CeO_2 was deposited between the FST layers with a dependence on $\boldsymbol{p}$ (2, 5, 10, and 20), where $\boldsymbol{p}$ is the number of laser pulses for the inserted CeO_2 (laser energy density of 1.5 J/cm^2 and a repetition rate of 1 Hz). The target changing time to switch between the FST and CeO_2 targets was 10 s, which was the drive time when the laser was turned off and then on again. The composition of the FST thin film was considered to be approximately $FeSe_{0.7}Te_{0.3}$, based on our previous report[11].

Characterization

To characterize the crystal structure, the θ–2θ, azimuthal phi, and rocking curve were measured using a four-circle XRD (PANalytical, X'Pert pro, $\lambda = 1.5406$ Å). We also performed an additional θ–2θ scan in beamline 3 A of the Pohang Accelerator Laboratory with a six circle XRD ($\lambda = 1.148$ Å). The STEM images and energy dispersive spectroscopy (EDS) maps were obtained by a C_s-corrected FEI Titan Themis G2 at an accelerating voltage of 300 kV with a beam current of 70 pA, a convergence semiangle of 15 mrad, and a collection semiangle snap in the range of 80–379 mrad. To obtain GPA maps of the Ce-FST and P-FST thin films, the same parameters were used for all calculations (same Fourier vector, resolution: 5 nm, smoothing: 10 nm, color scale: −0.1–0.12). The resistivity–temperature measurements were performed using a physical property measurement system (Quantum Design). T_c^{onset} and T_c^{zero} were determined using the 0.9 ρ_n criterion and 0.01 ρ_n criterion, respectively, where ρ_n is the resistivity at 23 K. The magnetization J_c was measured using a vibrating sample magnetometer (VSM, Oxford) by applying a magnetic field perpendicular to the film. This parameter was estimated using the Bean model for a thin film: $J_c = 15\Delta M/Vr$, where V is the thin film volume in cubic centimeters, r is the equivalent radius of the sample size ($\pi r^2 = a \times b$; a and b are the width and length of the sample, respectively), and ΔM is the width of the magnetic moment from the M–H loop (for further information, see Supplementary Fig. S1). The transport J_c is obtained by direct transport measurement of the patterned FST sample using a standard four-probe method.

Results and discussion

Crystalline phases

Figure 1 shows a schematic diagram of two different Ce-FST thin films. First, if the amount of inserted CeO_2 is

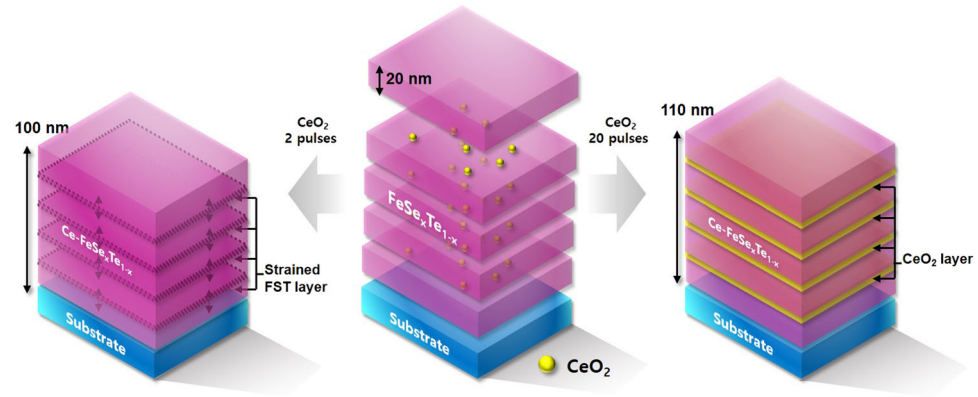

Fig. 1 Schematic of the two types of Ce-FST thin films. An infinitesimal amount of CeO_2 (2 ***p***) is injected at the interface between each FST layer to form nanostrained FST (left side). Sufficient CeO_2 (20 ***p***) is injected at the interface between each FST layer to form a CeO_2 layer (right side). The thickness of each FST layer is 20 nm, and the total thickness is 100–110 nm.

very small (2 ***p***, smaller than 0.5 unit cell), nanoscale defects can be formed inside the FST thin film, not the CeO_2 layer, given that the inserted 2 ***p*** CeO_2 is an infinitesimal amount that is insufficient to form nucleation clusters or layers inside an FST. These nanoscale defects can generate nanostrain inside an FST thin film (left side of Fig. 1). The mechanism is discussed later in detail. If the inserted CeO_2 (20 ***p***, 2.5 unit cell) is sufficient to form a CeO_2 layer in an FST thin film, a CeO_2 layer is formed between the FST layers without nanostrain (right side of Fig. 1). Thus, a 20 ***p*** Ce-FST thin film forms a superlattice FST thin film with CeO_2.

We performed a θ–2θ scan using XRD to identify the out-of-plane crystalline qualities of the Ce-FST thin films. Figure 2a shows the out-of-plane θ–2θ XRD spectra of the P-FST and Ce-FST thin films dependent on ***p*** (2, 5, 10, and 20). The θ–2θ scans clearly show only (00*l*) peaks for Ce-FST thin films with CaF_2 (00*l*) peaks. However, there are no other phase peaks present despite the periodically injected CeO_2 because the amount of CeO_2 inserted is too small to be measured by XRD. Figure 2b shows an enlarged section of Fig. 2a close to the (001) peak of the Ce-FST thin films. The (001) peak of 2 ***p*** Ce-FST is noticeably shifted more to the left than that of P-FST, indicating that 2 ***p*** Ce-FST experiences tensile strain along the *c*-axis. Intriguingly, the degree of shift of the (001) peak returns to zero with increasing ***p***. This result indicates that the strain relaxes in Ce-FST thin films with increasing ***p***. Additionally, the same shift tendency is observed in other 00*l* peaks in Ce-FST thin films (for further information, see Supplementary Fig. S2).

We additionally measured the θ–2θ of the 2 ***p*** Ce-FST and 20 ***p*** Ce-FST thin films using a synchrotron-based XRD to further verify the crystalline structure (for further information, see Supplementary Fig. S3). As shown in Fig. S3, only (00*l*) peaks are observed in both the 2 ***p*** Ce-FST and 20 ***p*** Ce-FST thin films, and the (001) peaks display satellite peaks, which have been generally observed in superlattice thin films[4]. Since 20 ***p*** Ce-FST thin films can have a superlattice structure with CeO_2, satellite peaks can be observed. However, in the 2 ***p*** Ce-FST thin film, it is difficult to form a superlattice structure with the formation of an intact CeO_2 layer in the FST matrix because a trace amount of CeO_2 is injected into the FST matrix. Thus, we speculate that the satellite peaks of the 2 ***p*** Ce-FST thin film are due to small changes, such as nanostrain at the interfaces between the FST layers.

Additionally, we measured the rocking curve of the (001) reflection of both the P-FST and 2 ***p*** Ce-FST thin films using four circles of XRD to compare the out-of-plane crystalline qualities and the mosaicity (Fig. 2c). The calculated full-width at half-maximum (FWHM) of the (001) reflection is 0.67° for the 2 ***p*** Ce-FST and 0.55° for the P-FST. The difference between the FWHMs of the P-FST and 2 ***p*** Ce-FST thin films is minimal, and the FWHM of 2 ***p*** Ce-FST is similar to those of other reported $FeSe_xTe_{1-x}$ thin films[5,9,11]. This result indicates that the 2 ***p*** Ce-FST thin film grew well along the *c*-axis despite the insertion of oxide materials into the FST matrix.

To confirm the in-plane texture and epitaxial quality, we performed an azimuthal phi scan using four circles of XRD. Figure 2d indicates the azimuthal ϕ scan of the (113) peak from the CaF_2 substrate and the (112) peak from the 2 ***p*** Ce-FST thin film. The ϕ scan of the 2 ***p*** Ce-FST thin film shows clear four peaks with 90° intervals without extra broader intermediate-angle peaks. These peaks are 45° with respect to the CaF_2 (113) peaks because the [100] FST is parallel to the [110] CaF_2. These results indicate that 2 ***p*** Ce-FST has the characteristics of a genuine epitaxial film with excellent in-plane texture.

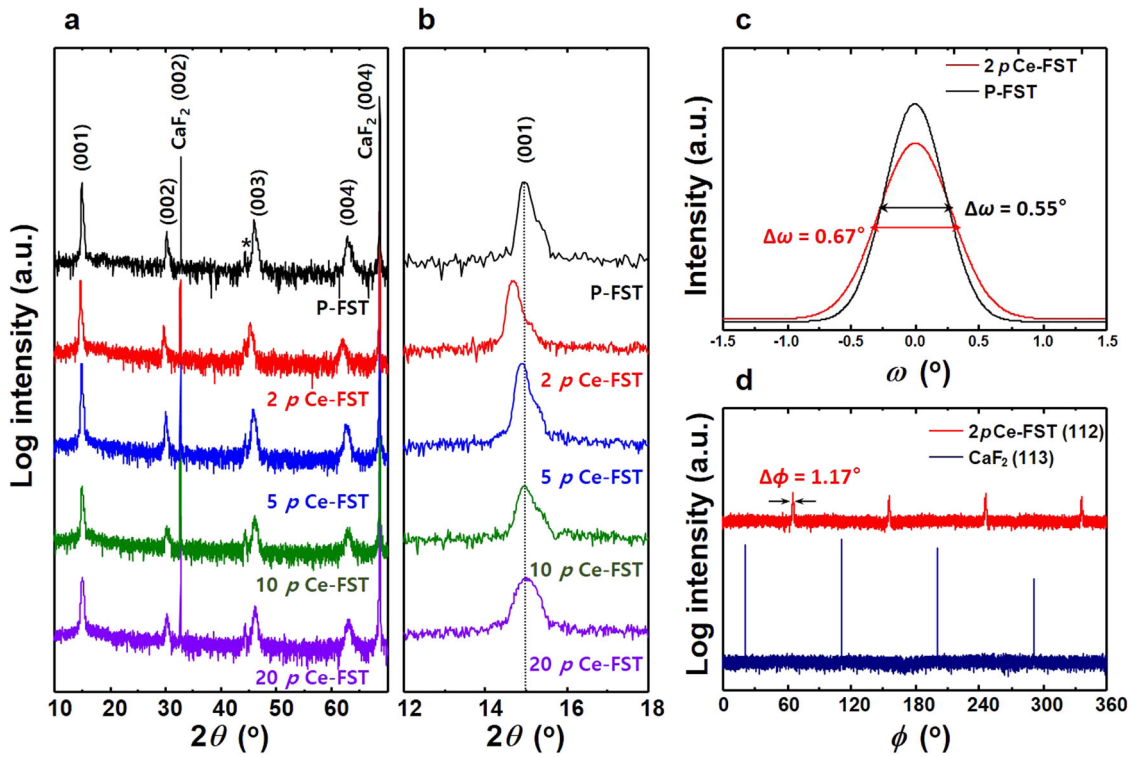

Fig. 2 XRD spectra of FST thin films for structure analysis. a Out-of-plane θ–2θ XRD spectra of the P-FST and Ce-FST thin films grown on CaF_2. **b** Enlarged FST (001) reflection of **a**. **c** Rocking curve of (001) reflection of the 2 ***p*** Ce-FST and the P-FST thin films. Here, $\Delta\omega$ indicates the FWHM of the (001) reflection of both films. **d** Azimuthal ϕ scan of the 2 ***p*** Ce-FST (113) and CaF_2 (112). * indicates an artifact peak from XRD equipment.

Strain analysis

To determine the nanoscale strain caused by the infinitesimal CeO_2 injection at the interface of each FST layer, we analyzed atomic-resolution-STEM images of the 2 ***p*** Ce-FST thin film. Figure 3a shows a cross-sectional atomic-resolution-STEM image of the 2 ***p*** Ce-FST thin film. As shown in Fig. 3a, no other dominant phases, such as CeO_2 particles, are observed except for the FST phase. Although we double checked for the presence of CeO_2 particles in the 2 ***p*** Ce-FST thin film, there are no CeO_2 layers, CeO_2 particles, or large-scale defects present (for further information, see Supplementary Fig. S4). However, fine bright lines are observed at 20-nm vertical intervals in the 2 ***p*** Ce-FST thin film. To analyze the fine bright lines in the 2 ***p*** Ce-FST thin films, we performed GPA based on the atomic-resolution-STEM image in Fig. 3a. GPA is generally used to show strain distributions and to determine the deformation of the lattice constant in crystalline structures[29]. Figure 3b shows an extracted strain map of the out-of-plane strain (ε_{zz}) of the identical region in Fig. 3a. The GPA map undoubtedly displays a strained region with 20-nm vertical intervals; the thickness of the nanostrained region is approximately 5–10 nm. To further analyze the strain, we plotted the line profile of the strain of the 2 ***p*** Ce-FST thin film based on the GPA results. As shown in Fig. 3c, nanostrains are observed with 20-nm vertical intervals. This nanostrain is tensile strain ($\varepsilon_{zz} \cong 0.02$) along the *c*-axis, and the position of the nanostrain agrees well with the location of the site where we intentionally inserted CeO_2.

For a more accurate comparison, we performed STEM analysis of the P-FST and 20 ***p*** Ce-FST thin films. The P-FST thin film exhibits a relatively clear phase, as shown in Fig. 3d; there is no particular strain field in the out-of-plane GPA strain map from the atomic-resolution-STEM image of the P-FST film (Fig. 3e). Figure 3f shows the line profile of the out-of-plane strain of the P-FST thin film. As shown in Fig. 3f, the strain in the P-FST thin film fluctuates around zero.

The 20 ***p*** Ce-FST thin film exhibits a clear CeO_2 layer between the 20-nm intervals of FST layers (Fig. 3g). Figure 3h shows an out-of-plane GPA image of the 20 ***p*** Ce-FST thin film. Figure 3i shows a line profile of the out-of-plane strain in the 20 ***p*** Ce-FST thin film. The large strain contrast at the CeO_2 layer in Fig. 3h, i is an artifact that is caused by the structural difference between FST and CeO_2. Relatively small strain fields (<0.02) are irregularly observed near the CeO_2 layer in the GPA map of the 20 ***p*** Ce-FST thin film. Interestingly, nanostrain is observed in the STEM image of the 2 ***p*** Ce-FST thin film, although

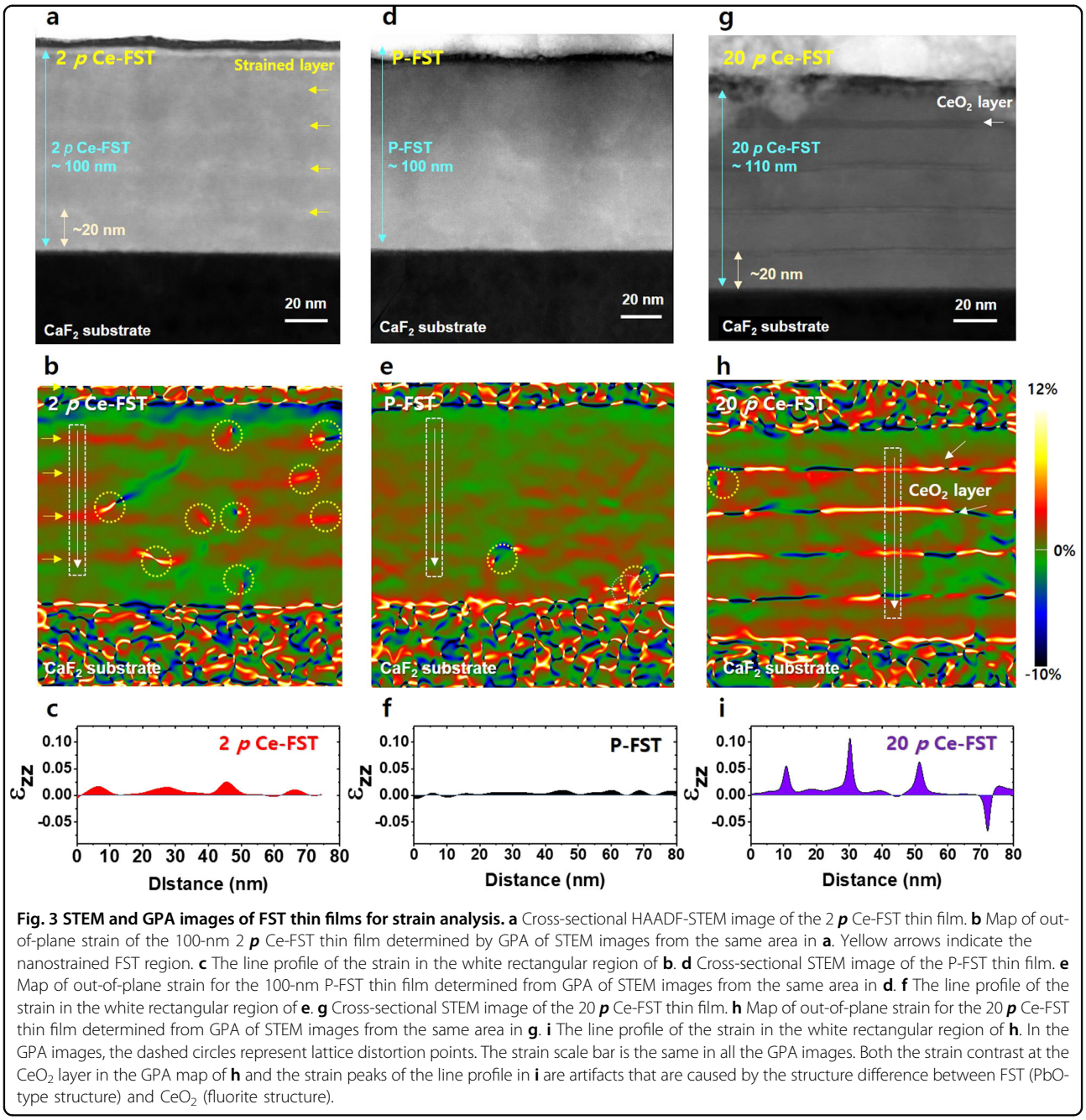

Fig. 3 STEM and GPA images of FST thin films for strain analysis. a Cross-sectional HAADF-STEM image of the 2 ***p*** Ce-FST thin film. **b** Map of out-of-plane strain of the 100-nm 2 ***p*** Ce-FST thin film determined by GPA of STEM images from the same area in **a**. Yellow arrows indicate the nanostrained FST region. **c** The line profile of the strain in the white rectangular region of **b**. **d** Cross-sectional STEM image of the P-FST thin film. **e** Map of out-of-plane strain for the 100-nm P-FST thin film determined from GPA of STEM images from the same area in **d**. **f** The line profile of the strain in the white rectangular region of **e**. **g** Cross-sectional STEM image of the 20 ***p*** Ce-FST thin film. **h** Map of out-of-plane strain for the 20 ***p*** Ce-FST thin film determined from GPA of STEM images from the same area in **g**. **i** The line profile of the strain in the white rectangular region of **h**. In the GPA images, the dashed circles represent lattice distortion points. The strain scale bar is the same in all the GPA images. Both the strain contrast at the CeO_2 layer in the GPA map of **h** and the strain peaks of the line profile in **i** are artifacts that are caused by the structure difference between FST (PbO-type structure) and CeO_2 (fluorite structure).

there are no CeO_2 layers or particles visible. Thus, it is important to demonstrate why the injected trace amount of CeO_2 forms nanostrain in the FST matrix and why there are no CeO_2 particles in the 2 ***p*** CeO_2 FST thin film.

In general, nanostrain is induced at various types of defect perimeters[16,18–21]. Interestingly, lattice distortion points (dashed circle in GPA maps of Fig. 3) such as dislocation cores and damaged FST layers are prominently observed in the nanostrain region in the GPA image of the 2 ***p*** Ce-FST thin film. Additionally, there are a few nanoscale defects that are formed irrespective of CeO_2 insertion in the FST thin films, as shown in Fig. 3d. These nanoscale defects can cause nanostrain in FST thin films. However, it is difficult to form nanostrain over a broad region by means of only these nanoscale defects because these defects form a localized strain field[18].

To further understand the origin of the nanostrained region, we analyzed an enlarged STEM image of the nanostrained region with no lattice distortion points using EDS mapping. Figure 4a–c shows different STEM images

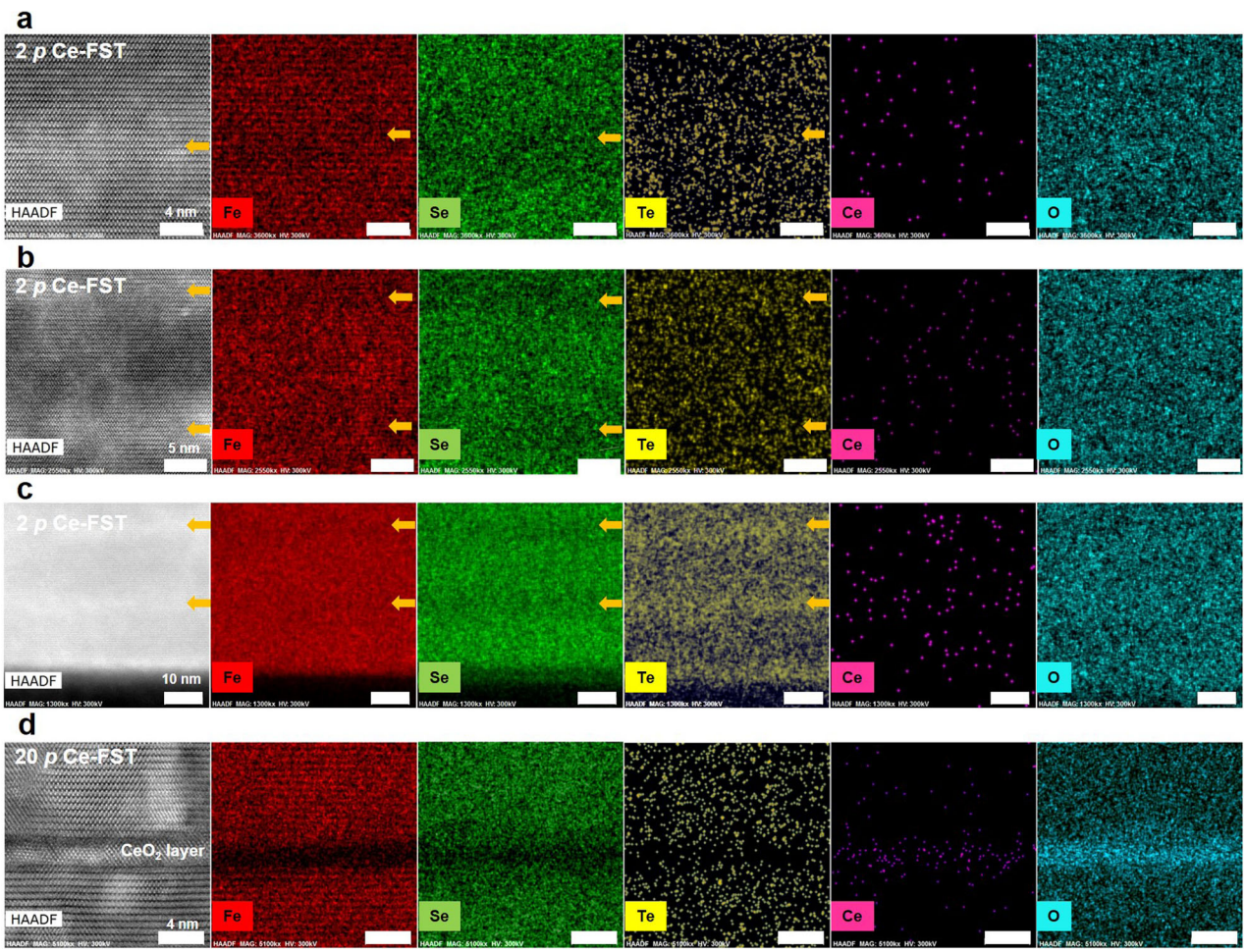

Fig. 4 Comparison between nanostrain and CeO_2 layer using STEM and EDS analysis. a–c Cross-sectional HAADF-STEM image of each different nanostrained region in the 2 ***p*** Ce-FST thin film with EDS maps of different types of atoms (Fe, Se, Te, Ce, and O) from the same area as that in the STEM images. **d** Cross-sectional HAADF-STEM image of the CeO_2 layer in the 20 ***p*** Ce-FST thin film with EDS maps of different types of atoms from the same area as that in the STEM image. Yellow arrows indicate the nanostrained regions.

of the 2 ***p*** Ce-FST thin film with EDS mapping results for different types of atoms, i.e., Fe, Se, Te, Ce, and O. Figure 4d shows a STEM image of the 20 ***p*** Ce-FST thin film with EDS mapping results for different types of atoms, i.e., Fe, Se, Te, Ce, and O. As shown in Fig. 4d, a CeO_2 layer is certainly observed in the 20 ***p*** Ce-FST thin film. The inserted CeO_2 was epitaxially grown with the relation (001)[110]FST || (001)[100]CeO_2. Both Ce and O are strongly detected around the CeO_2 layer in the EDS map of 20 ***p*** Ce-FST, whereas there are no Ce or O signals around the nanostrained region in the EDS maps of the 2 ***p*** Ce-FST thin film (Fig. 4a–c).

One interesting discovery is that not only fine decreases in both the Se and Fe ratios but also a fine increase in the Te ratio are observed in the nanostrained region in the EDS maps of the 2 ***p*** Ce-FST thin film when these EDS maps are analyzed using plot profiles (for further information, see Supplementary Fig. S5). The decrease in the Se ratio can cause an increase in the lattice constant[11]. This result indicates that nanostrain can be induced near the Se-deficient region that is generated by infinitesimal CeO_2 insertion.

Thus, it is important to demonstrate why Se deficiency is observed in nanostrained regions without residual CeO_2 particles. In the PLD system, the laser ablation of the target forms a plume that contains ionized species with high kinetic energy. These ionized energetic species cause resputtering and the formation of fine defects on the surface in the initial stage before these species form clusters or layers[30]. In this resputtering stage, it is impossible for the inserted CeO_2 to form an intact CeO_2 layer; instead, resputtering forms nanoscale defects and damaged FST layers (or a transition layer). These phenomena are observed in not only our 20 ***p*** Ce-FST thin

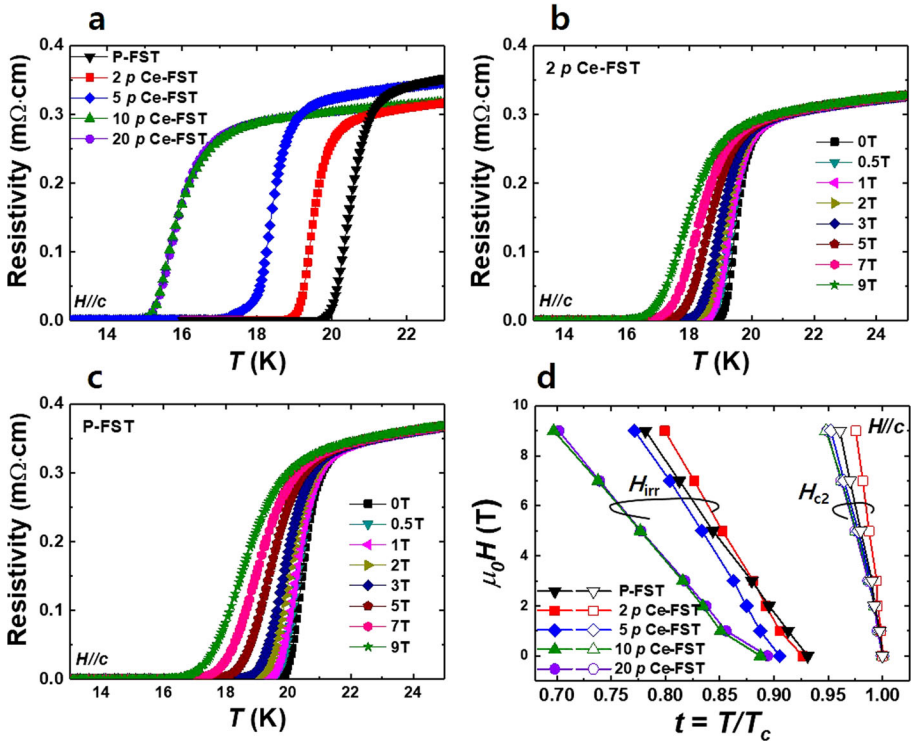

Fig. 5 T_c of FST thin films. a Temperature dependence of the resistivity of the P-FST and Ce-FST thin films. Temperature dependence of the resistivity of **b** the 2 ***p*** Ce-FST thin film and **c** the P-FST thin film depending on applied magnetic fields. **d** Upper-critical field [$H_{c2}(T)$] and irreversibility field [$H_{irr}(T)$] as a function of normalized temperature ($t = T/T_c$) for the Ce-FST and P-FST thin films. Each point shows the decreases in drops to 0.9 of the normal resistivity (ρ_n) and 0.01 of ρ_n. ρ_n is the resistivity of the normal states (ρ(23 K)) of the P-FST and Ce-FST thin films.

film, as shown in Fig. 4d, but also in other studies when a CeO_2 layer is deposited into or onto an FST thin film[26,27,31]. Furthermore, Se deficiency can be generated in the resputtering stage, provided that the atomic ratio of FST abnormally changes during thin film growth because of instability in the Fe–Se bonding[11]. Collectively, nanostrain can be induced by nanoscale defects, such as lattice distortion points, a damaged FST layer, and Se deficiency, that are formed by inserting an infinitesimal amount of CeO_2.

Furthermore, we examined whether the formation of nanostrain is affected by pausing (10 s) for an exchange of the FST and CeO_2 targets because Se and Te are sensitive and volatile in FST thin films[11]. The paused FST thin film was fabricated following the same fabrication process as that of the 2 ***p*** Ce-FST thin film except for CeO_2 injection; the CeO_2 plume was screened during the laser ablation of the CeO_2 target. The θ–2θ scan of the paused FST thin film using synchrotron-based XRD shows well-oriented (001) peaks without satellite peaks, indicating that the pausing time has a negligible effect on the formation of nanostrain in the FST matrix (for further information, see Supplementary Fig. S3).

Superconductivity measurements

We measured the temperature dependence of the resistivity to obtain the T_c to compare the superconducting properties of the P-FST and Ce-FST thin films (Fig. 5a). The measured T_c^{onset} values are 21.3, 20.4, 19.0, 16.9, and 16.7 K for the P-FST, 2 ***p*** Ce-FST, 5 ***p*** Ce-FST, 10 ***p*** Ce-FST, and 20 ***p*** Ce-FST thin films, respectively. In particular, the T_c values of the FST thin films decrease with increasing ***p*** of CeO_2. The primary reason for the T_c degradation in the Ce-FST thin films is the degradation of the crystalline quality with increasing amounts of inserted CeO_2 (for further information, see Supplementary Fig. S6). Figure 5b, c, and S7 (for further information, see Supplementary S7) show the resistivity as a function of temperature up to 9 T with $H//c$ for the 2 ***p*** Ce-FST, P-FST, and other Ce-FST thin films, respectively. Interestingly, the suppression of the T_c of the 2 ***p*** Ce-FST thin film ($\Delta T_{c,field}^{zero} = 2.6$ K), which is dependent on the magnetic field ($\Delta T_{c,field}^{zero} = T_{c,9T}^{zero} - T_{c,0T}^{zero}$), is lower than that of the P-FST thin film ($\Delta T_{c,field}^{zero} = 3.2$ K); the measured $T_{c,0T}^{zero}$ and $T_{c,9T}^{zero}$ are 19.8 and 16.6 K, respectively, for the P-FST thin film and 18.9 and 16.3 K, respectively, for the 2 ***p*** Ce-FST thin film. This result indicates that the 2 ***p*** Ce-FST

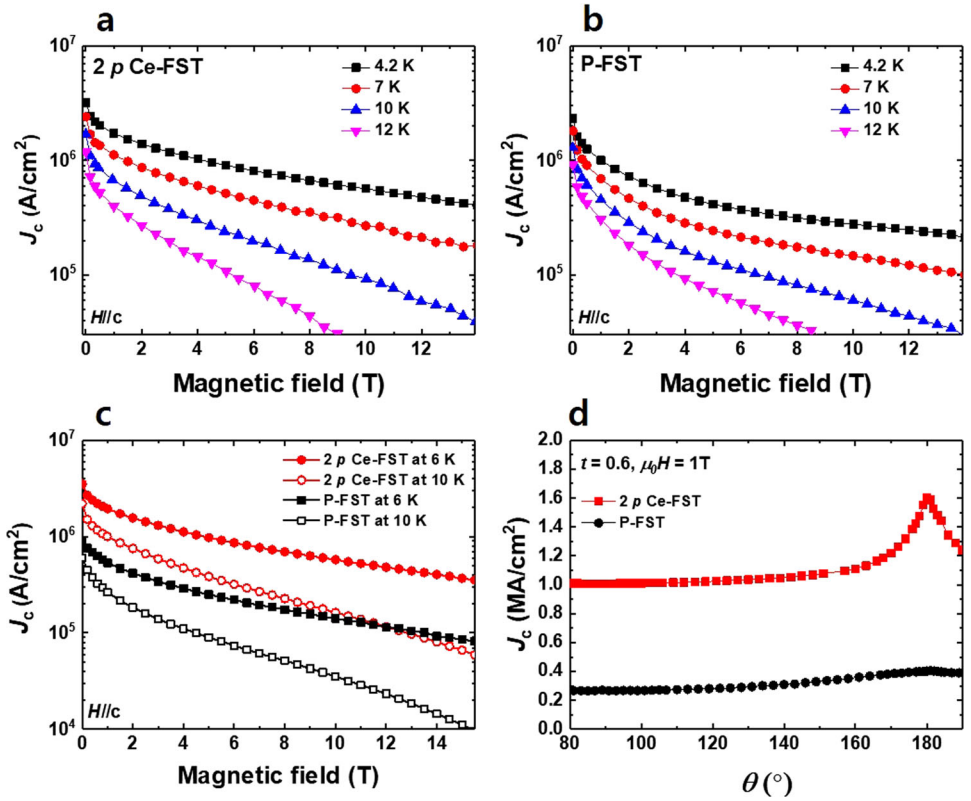

Fig. 6 J_c of 2 *p* and P-FST thin films. Magnetization J_c as a function of the magnetic field ($H//c$) of **a** the 2 ***p*** Ce-FST and **b** the P-FST thin films, which was derived from half magnetization loops at different temperatures (4.2, 7, 10, and 12 K). **c** Transport J_c as a function of magnetic field ($H//c$) for both P-FST and 2 ***p*** Ce-FST thin films up to 15 T at 6 and 10 K. **d** Angular dependence of the transport J_c of 2 ***p*** Ce-FST and P-FST evaluated at a constant reduced temperature t (T/T_c) ~ 0.6.

thin film has a lower magnetic field dependence than the P-FST thin film, although the T_c of 2 ***p*** Ce-FST is lower than that of the P-FST thin film.

We estimated the H_{irr} and H_{c2} of the Ce-FST and P-FST thin films using the 0.01 ρ_n criterion and the 0.9 ρ_n criterion with $\rho_n = \rho(23\,K)$ as a function of the normalized temperature ($t = T/T_c^{onset}$) to characterize the temperature dependence of the characteristic fields. (Fig. 5d). The improved H_{irr} of 2 ***p*** Ce-FST is indicative of the beneficial effect of the periodic nanostrained region with nanoscale defects as pinning centers under high magnetic fields. In contrast, the H_{c2} and H_{irr} of other Ce-FST (5, 10, and 20 ***p***) are degraded after CeO_2 insertion, indicating that CeO_2 particles and layers can degrade H_{irr} and H_{c2} in an FST thin film.

The J_c of both the 2 ***p*** Ce-FST and the P-FST thin films was measured to verify the effect of the nanostrain as a pinning center on the supercurrents in the FST thin films (Fig. 6). Figure 6a, b shows the magnetic field dependence magnetization J_c of the 2 ***p*** Ce-FST and the P-FST thin films at various temperatures (4.2, 7, 10, and 12 K) up to 13 T ($H//c$). The magnetization J_c of the 2 ***p*** Ce-FST thin film has a value of 3.2 MA/cm^2 in a self-field and 0.44 MA/cm^2 under 13 T at 4.2 K. The self-field J_c of the 2 ***p*** Ce-FST thin film is the highest value for an iron-chalcogenide superconductor to the best of our knowledge[15,32]. The magnetization J_c of the P-FST thin film has a value of 2.3 MA/cm^2 in a self-field and 0.23 MA/cm^2 under 13 T at 4.2 K. The magnetization J_c of the P-FST thin film is similar to and higher than other reported values[15,16,27]. The transport J_c of both the P-FST and Ce-FST thin films was measured at 6 and 10 K to verify the magnetization J_c derived using the Bean model (Fig. 6c). The 2 ***p*** Ce-FST shows a transport J_c of 3.5 MA/cm^2 in a self-field and of 0.44 MA/cm^2 under 13 T at 6 K, which is reasonably similar to the magnetization J_c of the Ce-FST thin film at 4.2 K. The P-FST shows a transport J_c of 0.91 MA/cm^2 in a self-field and of 0.10 MA/cm^2 under 13 T at 6 K, which is similar to the magnetization J_c of the P-FST thin film at 7 K.

Additionally, the J_c enhancement was calculated to confirm the effect of nanostrain in detail based on the magnetization J_c (for further information, see Supplementary Fig. S8). The J_c enhancement of 2 ***p*** Ce-FST compared with that of P-FST increases from 40% to 120% up to 5 T and gradually decreases under a high magnetic

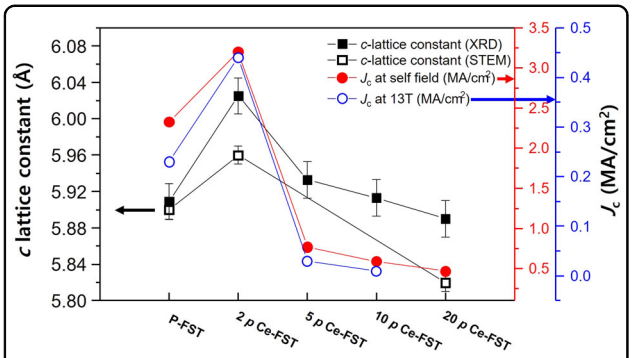

Fig. 7 Relationship between J_c and nanostrain. As a function of *p* in the FST thin films, *c*-lattice constants were calculated from STEM and XRD results, magnetization J_c under self-field, and magnetization J_c under 13 T.

field. These results clearly demonstrate that 2 ***p*** Ce-FST maintains a high J_c under a high magnetic field and a low magnetic field. Furthermore, we measured the angular dependence of the transport J_c of the 2 ***p*** Ce-FST and P-FST at a constant reduced temperature $T/T_c \sim 0.6$ to understand the pinning effects of nanostrain with nanoscale defects. As shown in Fig. 6d, the in-plane J_c is 48% higher than the perpendicular J_c in the P-FST thin films. The 2 ***p*** Ce-FST film shows an enhanced in-plane J_c of 1.6 MA/cm^2, which is 60% higher than the perpendicular J_c of 1.0 MA/cm^2 due to the in-plane pinning effect by the lateral nanostrain. Above all, nanostrain with other nanoscale defects improves the J_c of the 2 ***p*** Ce-FST film under all directions of magnetic field.

Relationship between nanostrain and J_c

Additionally, we plotted the lattice constant, *c*, and magnetization, J_c, at 4.2 K as a function of the ***p*** of inserted CeO_2 to further understand the relationship between nanostrain and J_c (Fig. 7). The lattice constants were obtained by the Nelson Riley method based on the XRD results and by fast Fourier transform analysis based on the STEM images (for further information, see Supplementary Figs. S9 and S10). The magnetization J_c of the Ce-FST thin films (2, 5, 10, and 20 ***p***) was measured at 4.2 K (for further information, see Supplementary Fig. S11). As shown in Fig. 7, the change in J_c follows the same tendency as the change in the lattice constant, *c*, which represents the change in strain. This tendency demonstrates that nanostrain is responsible for the enhanced J_c in the 2 ***p*** Ce-FST thin film.

To understand the pinning mechanism of the 2 ***p*** Ce-FST thin film, we plotted $J_c(t)/J_c(0)$ versus *t* for both the 2 ***p*** Ce-FST and P-FST thin films based on the magnetization J_c of both the 2 ***p*** Ce-FST and P-FST thin films (for further information, see Supplementary S12). Both the 2 ***p*** Ce-FST and P-FST thin films show the *δl*-pinning type, which is caused by fluctuations in the charge-carrier mean free path. We also calculated the scaled-volume pinning force (f_p) as a function of the normalized field (h); f_p is F_p/F_{p_max}, and h is H/H_{irr} (for further information, see Supplementary Fig. S12). In general, h values of 0.2 and 0.33 indicate a surface pinning geometry and point pinning geometry, respectively[33]. If the J_c of the 2 ***p*** Ce-FST thin film is improved by CeO_2 particles or other defects that cause point and volume pinning, the h value is shifted to 0.33. However, the h of f_p is approximately 0.2 in both the P-FST and 2 ***p*** Ce-FST thin films, indicating that the main pinning type in both the P-FST and 2 ***p*** Ce-FST thin films is surface pinning.

In a P-FST thin film that has a pure FST phase without defects, the interlayer spacing between Fe–Se(Te) planes can be an intrinsic pinning center due to the short coherence length of FST[34]. Since this interlayer spacing has a two-dimensional lateral geometry, the pinning type of the interlayer spacing in the P-FST thin film is surface pinning geometry. Interestingly, the 2 ***p*** Ce-FST thin film also has a surface pinning geometry even though its J_c is relatively improved compared with that of the P-FST thin film. This result means that the 2 ***p*** Ce-FST thin film has a pinning type similar to that of the P-FST thin film. The difference between the P-FST thin film and the 2 ***p*** Ce-FST thin film is that the *c*-lattice of the 2 ***p*** Ce-FST thin film is expanded by the nanostrain compared with that of the P-FST thin film, indicating that the interlayer spacing of the 2 ***p*** Ce-FST thin film at the nanostrained region is larger than that of the P-FST thin film. Thus, the interlayer spacing of 2 ***p*** Ce-FST can be a more effective pinning center than that of P-FST.

To evaluate the efficiency of our method, we compared the pinning characteristics with those of previous papers[14–16,35–38]. Figure 8a shows the transport J_c of 2 ***p*** Ce-FST and P-FST at 6 K for $H//c$ together with the J_c of other reported superconductors. The 2 ***p*** Ce-FST thin film exhibits a J_c higher than the other reported J_c of FST thin films[14–16,35–38]. We also estimated the pinning force (F_p) to characterize the effect of nanostrain with nanoscale defects. Figure 8b shows the magnetic field dependences of the vortex pinning force ($F_p = J_c \times B$) of both the 2 ***p*** Ce-FST and the P-FST thin films up to 13 T ($H//c$) at 6 K together with the reported F_p of other superconductors[14–16,35–38]. The 2 ***p*** Ce-FST and P-FST thin films show maximum pinning forces ($F_{p,max}$) of 57.8 GN/m^3 under 11.5 T and 14.2 GN/m^3 under 11 T at 6 K, respectively. In particular, the 2 ***p*** Ce-FST thin film shows an $F_{p,max} \sim 400\%$ higher than that of the P-FST thin film at 13 T ($H//c$). In addition, the 2 ***p*** Ce-FST thin film exhibits a higher F_p than the other reported FST, even though our samples were measured at a relatively higher temperature of 6 K.

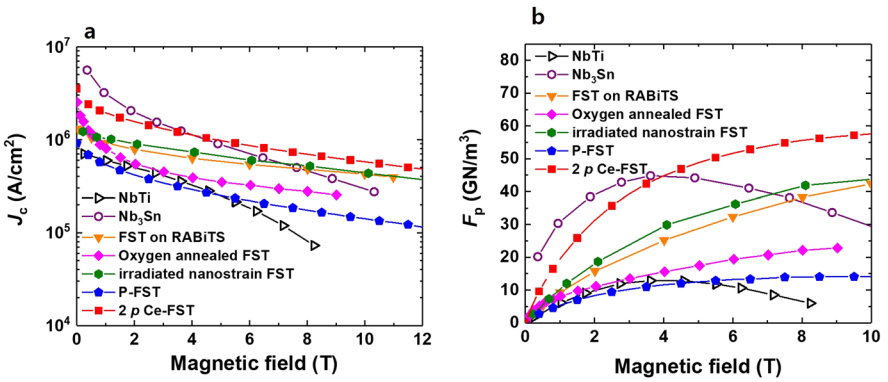

Fig. 8 J_c and F_p analysis of FST thin films. Dependences of transport J_c (**a**) and vortex pinning force F_p (**b**) on magnetic field for several high-field superconductors, including P-FST, 2 ***p*** Ce-FST (this work), FST on coated conductors (RABiTS), oxygen annealed FST, ion irradiated FST, Nb–Ti, and Nb_3Sn. J_c data of high-field superconductors at 4.2 K. Except for our samples, all the data are adopted from the literature[14–16,34–38].

Conclusions

Herein, we successfully induce nanostrain inside FST thin films via the injection of an infinitesimal amount of CeO_2 using S-PLD without additional postprocessing. Through STEM analysis with GPA and EDS, we demonstrate that the injected infinitesimal amount of CeO_2 forms nanoscale defects such as dislocation cores and Se deficiencies, which forms tensile nanostrain along the *c*-axis of the FST thin film. The nanostrain significantly improves the self-field transport J_c of the FST thin film from 0.91 MA/cm^2 up to 3.5 MA/cm^2 at 6 K, while minimizing the degradation of the T_c of the FST thin film. This study demonstrates that the formation of nanostrain using S-PLD is significantly effective toward achieving the ultimate goal of high magnetic field applications of iron chalcogenide. We also believe that this technique will be of great utility in inducing artificial nanoscale strains in other epitaxial chalcogenide thin films.

Acknowledgements

This work was supported by the Global Research Network program (2014S1A2A2028361), the Creative Materials Discovery Program (2017M3D1A1040828), the Basic Science Research Program (2016R1D1A1B03931748), and the International Cooperation Program (2018K2A9A1A06069211) through the National Research Foundation of Korea (NRF) and was funded by the Ministry of Science, ICT and Future Planning, the Ministry of Education and the GRI (GIST Research Institute) project through a grant provided by GIST. P.G. is grateful for the support from the National Key Research and Development Program of China (2016YFA0300804) and the National Science Foundation of China (51502007 and 51672007). A portion of this work was performed at the National High Magnetic Field Laboratory, which is supported by the National Science Foundation Cooperative Agreement Nos. DMR-1157490 and DMR-1644779 and the State of Florida.

Author details

[1]School of Materials Science and Engineering, Gwangju Institute of Science and Technology, Gwangju 61005, Republic of Korea. [2]Electron Microscopy Laboratory, and International Center for Quantum Materials, School of Physics, Peking University, 100871 Beijing, China. [3]Applied Superconductivity Center, National High Magnetic Field Laboratory, Florida State University, Tallahassee, FL 32310, USA. [4]Center for Quantum Materials and Superconductivity (CQMS) and Department of Physics, Sungkyunkwan University, Suwon 16419, Republic of Korea. [5]Department of Physics, Kyungpook National University, Daegu 41566, Republic of Korea. [6]Condensed Matter Physics and Materials Science Department, Brookhaven National Laboratory, Upton, NY 11973, USA

Conflict of interest

The authors declare that they have no conflict of interest.

Supplementary information is available for this paper at https://doi.org/10.1038/s41427-019-0186-y.

Received: 28 May 2019 Revised: 9 September 2019 Accepted: 30 October 2019.
Published online: 24 January 2020

References

1. Putti, M. et al. New Fe-based superconductors: properties relevant for applications. *Supercond. Sci. Technol.* **23**, 034003 (2010).
2. Gurevich, A. Iron-based superconductors at high magnetic fields. *Rep. Prog. Phys.* **74**, 124501 (2011).
3. Lee, S. et al. Template engineering of Co-doped $BaFe_2As_2$ single-crystal thin films. *Nat. Mater.* **9**, 397–402 (2010).
4. Lee, S. et al. Artificially engineered superlattices of pnictide superconductors. *Nat. Mater.* **12**, 392–396 (2013).
5. Yuan, P. et al. High performance $FeSe_{0.5}Te_{0.5}$ thin films grown at low temperature by pulsed laser deposition. *Supercond. Sci. Technol.* **28**, 065009 (2015).
6. Imai, Y. et al. Control of structural transition in $FeSe_{1-x}Te_x$ thin films by changing substrate materials. *Sci. Rep.* **7**, 46653 (2017).
7. Iida, K. et al. Oxypnictide SmFeAs(O,F) superconductor: a candidate for high–field magnet applications. *Sci. Rep.* **3**, 2139 (2013).
8. Braccini, V. et al. Highly effective and isotropic pinning in epitaxial Fe(Se,Te) thin films grown on CaF_2 substrates. *Appl. Phys. Lett.* **103**, 172601 (2013).
9. Bellingeri, E. et al. Tuning of the superconducting properties of $FeSe_{0.5}Te_{0.5}$ thin films through the substrate effect. *Supercond. Sci. Technol.* **25**, 084022 (2012).
10. Hsu, F.-C. et al. Superconductivity in the PbO-type structure α-FeSe. *Proc. Natl Acad. Sci. USA* **105**, 14262–14264 (2008).
11. Seo, S. et al. Origin of the emergence of higher T_c than bulk in iron chalcogenide thin films. *Sci. Rep.* **7**, 9994 (2017).

12. Imai, Y., Sawada, Y., Nabeshima, F. & Maeda, A. Suppression of phase separation and giant enhancement of superconducting transition temperature in $FeSe_{1-x}Te_x$ thin films. *Proc. Natl Acad. Sci. USA* **112**, 1937–1940 (2015).
13. Ge, J.-F. et al. Superconductivity above 100 K in single-layer FeSe films on doped $SrTiO_3$. *Nat. Mater.* **14**, 285 (2015).
14. Si, W. et al. High current superconductivity in $FeSe_{0.5}Te_{0.5}$-coated conductors at 30 tesla. *Nat. Commun.* **4**, 1347 (2013).
15. Zhang, C., Si, W. & Li, Q. Doubling the critical current density in superconducting $FeSe_{0.5}Te_{0.5}$ thin films by low temperature oxygen annealing. *Appl. Phys. Lett.* **109**, 202601 (2016).
16. Ozaki, T. et al. A route for a strong increase of critical current in nanostrained iron-based superconductors. *Nat. Commun.* **7**, 13036 (2016).
17. Massee, F. et al. Imaging atomic-scale effects of high-energy ion irradiation on superconductivity and vortex pinning in Fe(Se,Te). *Sci. Adv.* **1**, e1500033 (2015).
18. Llordes, A. et al. Nanoscale strain-induced pair suppression as a vortex-pinning mechanism in high-temperature superconductors. *Nat. Mater.* **11**, 329 (2012).
19. Rouco, V. et al. Nanostrain induced pinning in $YBa_2Cu_3O_{7-x}$ nanocomposites even close to the irreversibility line. *Supercond. Sci. Technol.* **25**, 122001 (2012).
20. Zeljkovic, I. et al. Nanoscale interplay of strain and doping in a high-temperature superconductor. *Nano Lett.* **14**, 6749–6753 (2014).
21. Lin, Y. et al. Atomic configuration of point defect clusters in ion-irradiated silicon carbide. *Sci. Rep.* **7**, 14635 (2017).
22. Ahmad, D. et al. Effect of proton irradiation on the fluctuation-induced magnetoconductivity of $FeSe_{1-x}Te_x$ thin films. *N. J. Phys.* **19**, 093004 (2017).
23. Mele, P. Superconducting properties of iron chalcogenide thin films. *Sci. Technol. Adv. Mater.* **13**, 054301 (2012).
24. Haugan, T., Barnes, P., Wheeler, R., Meisenkothen, F. & Sumption, M. Addition of nanoparticle dispersions to enhance flux pinning of the $YBa_2Cu_3O_{7-x}$ superconductor. *Nature* **430**, 867 (2004).
25. Kiessling, A. et al. Nanocolumns in $YBa_2Cu_3O_{7-x}$/$BaZrO_3$ quasi-multilayers: formation and influence on superconducting properties. *Supercond. Sci. Technol.* **24**, 055018 (2011).
26. Huang, J., Chen, L., Jian, J., Khatkhatay, F. & Wang, H. Nanostructured pinning centers in $FeSe_{0.1}Te_{0.9}$ thin films for enhanced superconducting properties. *Supercond. Sci. Technol.* **27**, 105006 (2014).
27. Chen, L. et al. Enhanced flux pinning properties in superconducting $FeSe_{0.5}Te_{0.5}$ thin films with secondary phases. *Supercond. Sci. Technol.* **25**, 025020 (2012).
28. Yuan, F. et al. The influence of the in-plane lattice constant on the superconducting transition temperature of $FeSe_{0.7}Te_{0.3}$ thin films. *AIP Adv.* **7**, 065015 (2017).
29. Hÿtch, M. J., Putaux, J.-L. & Pénisson, J.-M. Measurement of the displacement field of dislocations to 0.03 Å by electron microscopy. *Nature* **423**, 270 (2003).
30. Schneider, C. W. & Lippert, T. In: Schaaf P. (ed), *Laser Processing of Materials* 89–112 (Springer, 2010).
31. Huang, J. et al. Magnetic $(CoFe_2O_4)_{0.1}(CeO_2)_{0.9}$ nanocomposite as effective pinning centers in $FeSe_{0.1}Te_{0.9}$ thin films. *J. Phys.Condens. Matter* **28**, 025702 (2015).
32. Hänisch, J., Iida, K., Hühne, R. & Tarantini, C. Fe-based superconducting thin films—preparation and tuning of superconducting properties. *Supercond. Sci. Technol.* **32**, 093001 (2019).
33. Dew-Hughes, D. Flux pinning mechanisms in type II superconductors. *Philos. Mag.* **30**, 293–305 (1974).
34. Iida, K. et al. Intrinsic pinning and the critical current scaling of clean epitaxial Fe(Se,Te) thin films. *Phys. Rev. B* **87**, 104510 (2013).
35. Cooley, L., Lee, P. & Larbalestier, D. C. Flux-pinning mechanism of proximity-coupled planar defects in conventional superconductors: evidence that magnetic pinning is the dominant pinning mechanism in niobium-titanium alloy. *Phys. Rev. B* **53**, 6638 (1996).
36. Godeke, A. A review of the properties of Nb_3Sn and their variation with A15 composition, morphology and strain state. *Supercond. Sci. Technol.* **19**, R68 (2006).
37. Larbalestier, D. & West, A. New perspectives on flux pinning in Niobium-Titanium composite superconductors. *Acta Metall.* **32**, 1871–1881 (1984).
38. Scanlan, R., Fietz, W. & Koch, E. Flux pinning centers in superconducting Nb_3Sn. *J. Appl. Phys.* **46**, 2244–2249 (1975).